Regulatory Light Chain Mutants Linked to Heart Disease Modify the Cardiac Myosin Lever Arm

2 AUTHORS:

Thomas P Burghardt
Mayo Foundation for Medical Education and R…

111 PUBLICATIONS **2,470** CITATIONS

Laura A Sikkink
Mayo Foundation for Medical Education and R…

16 PUBLICATIONS **367** CITATIONS

Regulatory Light Chain Mutants Linked to Heart Disease Modify the Cardiac Myosin Lever Arm

Thomas P. Burghardt*[,†,‡] and Laura A. Sikkink[†]

[†]Department of Biochemistry and Molecular Biology and [‡]Department of Physiology and Biomedical Engineering, Mayo Clinic Rochester, Rochester, Minnesota 55905, United States

S *Supporting Information*

ABSTRACT: Myosin is the chemomechanical energy transducer in striated heart muscle. The myosin cross-bridge applies impulsive force to actin while consuming ATP chemical energy to propel myosin thick filaments relative to actin thin filaments in the fiber. Transduction begins with ATP hydrolysis in the cross-bridge driving rotary movement of a lever arm converting torque into linear displacement. Myosin regulatory light chain (RLC) binds to the lever arm and modifies its ability to translate actin. Gene sequencing implicated several RLC mutations in heart disease, and three of them are investigated here using photoactivatable GFP-tagged RLC (RLC-PAGFP) exchanged into permeabilized papillary muscle fibers. A single-lever arm probe orientation is detected in the crowded environment of the muscle fiber by using RLC-PAGFP with dipole orientation deduced from the three-spatial dimension fluorescence emission pattern of the single molecule. Symmetry and selection rules locate dipoles in their half-sarcomere, identify those at the minimal free energy, and specify active dipole contraction intermediates. Experiments were performed in a microfluidic chamber designed for isometric contraction, total internal reflection fluorescence detection, and two-photon excitation second harmonic generation to evaluate sarcomere length. The RLC-PAGFP reports apparently discretized lever arm orientation intermediates in active isometric fibers that on average produce the stall force. Disease-linked mutants introduced into RLC move intermediate occupancy further down the free energy gradient, implying lever arms rotate more to reach stall force because mutant RLC increases lever arm shear strain. A lower free energy intermediate occupancy involves a lower energy conversion efficiency in the fiber relating a specific myosin function modification to the disease-implicated mutant.
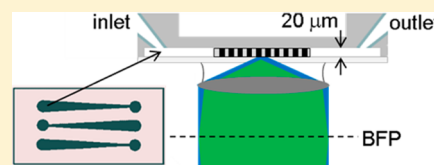
Myosin is an energy transducer converting ATP free energy into mechanical work. It has a globular head or subfragment 1 (S1) and a linear tail domain for the assembly of myosin into thick filaments that interdigitate with actin thin filaments in striated muscle. Myosin's function is to power the relative sliding of thick and thin filaments during contraction. S1 contains the actin binding site and a lever arm whose rotary movement while myosin is strongly actin bound cyclically generates tension to move the load as shown in Figure 1. The lever arm converts torque generated in the motor into the linear displacement characteristic of contraction and undergoes shear strain due to the load resisting translation. Strain under load is shared among the lever arm and the myosin light chains, essential and regulatory, that bind to the lever arm. In vitro evidence indicates human cardiac regulatory light chain (HCRLC) probably stabilizes the lever arm structure[1] and that HCRLC mutants implicated in disease lower velocity, force, and strain sensitivity,[2] suggesting they alter lever arm processing of shear stress.

Photoactivatable green fluorescent protein (PAGFP) linked to the C-terminus of HCRLC (HCRLC-PAGFP) is expressed in bacteria and exchanged with >50% efficiency with the endogenous RLC in permeabilized porcine cardiac papillary muscle fibers. Upon photoactivation, a sparse population of tagged myosins fluoresce. We detect them individually despite the high myosin concentration in the sarcomere. Single molecules emit in a pattern uniquely representing the PAGFP

dipole moment orientation as it tracks lever arm orientation.[3] Previously, we observed lever arm orientation from single myosins in relaxation, rigor, and isometric contraction.[4] The active isometric cross-bridge had apparently quantized lever arm orientations, suggesting the presence of substates in its force generation cycle.

Single-molecule detection (in principal) samples each state of a system addressing problems inherent to an ensemble average approach, although practical limitations persist.[5] Here we measured the PAGFP orientation on myosin in the muscle under rigor, active isometric, and relaxed conditions representing different free energy and actin attachment states. In a basic contraction mechanism, the myosin states transit from one to another producing force as the actin-attached myosin rotates a lever arm performing the power stroke. Direct single-molecule power stroke transition detection is beyond current capabilities. Instead, we use dispersion in the active isometric fiber to represent cross-bridge states at the high-free energy side of the transition and the unique low-free energy rigor state to represent the low-free energy side. We do not image the same single molecule across the three physiological states for two reasons. The first is that the fiber moves from its relaxed or
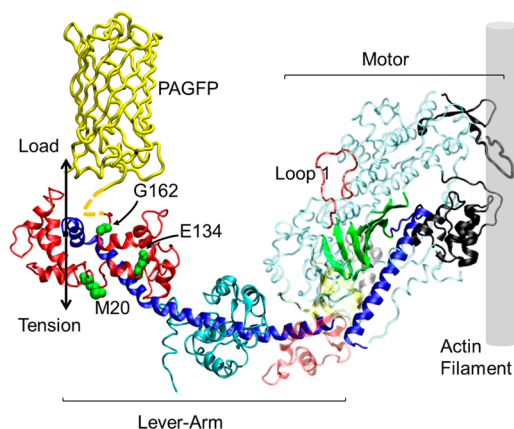
Figure 1. Human β-cardiac myosin S1 motor binds the actin filament and generates tension with the lever arm swing. In a muscle fiber, the lever arm links to the myosin filament where load and tension vectors are shown. Regulatory light chain (HCRLC in dark red) indicates positions 20, 134, and 162 with mutations implicated in HCM. PAGFP is linked to the light chain (dashed yellow linker near G162) and reports lever arm orientation. ELC is colored cyan. In the motor, black regions are the actin binding sites, the blue α-helix is the switch 2 helix, and the green β-sheet is the active site with an entrance at loop 1.

rigor position while the activated fiber becomes isometric and again as the active isometric fiber is returned to a resting state. The movement makes recovery of the single molecule of interest uncertain and impractical. The second is that rigor tension imposition from relaxed or active states produces rigor dispersion in which an unknown subset of rigor cross-bridges reach their unique free energy minimum. To manage these contingencies, we compute the set of likely transitions linking different single molecules in disperse active isometric states to their unique minimal free energy rigor configuration. Compatible single molecules conform to a symmetry rule associating myosin molecules in the same half-sarcomere and a selection rule associating the disperse active states with their lowest-free energy rigor-state partner. Overall, this approach is practical and avoids the rigor dispersion ambiguity. Results are from identical permeabilized fibers except for the introduction of HCRLC point mutations.

Here we report findings on the cardiac papillary muscle fiber system perturbed by three hypertrophic cardiomyopathy (HCM) -linked mutations of HCRLC (gene MYL2).[6] Mutants M20L, E134A, and G162R span the length of the regulatory light chain. They survey HCRLC for sensitivity to mutation with M20 near the phosphorylation site at Ser15,[7] E134 a charged residue probably participating in HCRLC–lever arm binding,[8] and G162 at the C-terminus adjacent to the myosin short α-helix at the end of, and orthogonal to, the lever arm long α-helix. Measurements with exchanged HCRLC-PAGFP show disease-linked mutants invert intermediate-state occupation favoring a lower free energy in the active cycle when compared to the wild type (WT). Lower-free energy intermediate occupancy causes lower energy conversion efficiency in the fiber. These findings demonstrate a myosin functional modification characterized at the single-molecule level, and in the context of the crowded muscle fiber, linking the HCM phenotype to a lower efficiency for ATP free energy conversion to mechanical work.

METHODS

Preparation of HCRLC. cDNA of WT MYL2 was a gift from D. Szczesna-Cordary (University of Miami, Miami, FL). HCRLC-GFP was constructed as previously described.[9] Mutagenesis of GFP to PAGFP was also previously described.[10] HCRLC mutants M20L, E134A, and G162R were made in the HCRLC and HCRLC-PAGFP pET3d plasmid using the QuikChange site-directed mutagenesis kit (Agilent Technologies, Santa Clara, CA). Expressed protein was purified and used for fiber exchange as described previously.[4] Protein concentrations used in the fiber exchange were 62.5−108.1 μM.

Solutions. Fiber solutions are based on the protocol of Szczesna-Cordary et al.[11] and were prepared exactly as described previously.[4] Rigor, relax, and active solutions were adjusted to an ionic strength of 150 mM by varying the potassium propionate (KPr) concentration and using the program FIBER PCA.xls to estimate total concentrations of species.[12] Relax and active solutions have pCa values of 8 and 4, respectively.

Permeabilized Fiber Preparation. Fiber preparation, dissection, light chain exchange, and tension measurements were conducted as previously described.[4] Fiber bundles used in tension or microscope experiments consisted of 3−10 fibers each (width of 50−100 μm) 2 mm in length. After tension measurements had been completed, fibers were severed from the tension transducer and prepared for microscope experiments or protein extraction and sodium dodecyl sulfate−polyacrylamide gel electrophoresis (SDS−PAGE) as described previously.[4]

SDS−PAGE from Fiber-Extracted Proteins. Exchanged fibers were tension tested and prepared as described above, and then proteins were extracted and subjected to SDS−PAGE analysis to measure light chain extraction and reconstitution efficiency as described previously.[4] The summary of SDS−PAGE results from tagged HCRLC (WT-PAGFP, M20L-PAGFP, E134A-PAGFP, and G162R-PAGFP) indicates fractional endogenous light chain removal of 0.53 ± 0.03, 0.34 ± 0.20, 0.58 ± 0.16, and 0.60 ± 0.06, respectively, and full replacement to within error.

Microfluidic Chamber for TIRF and SHG Microscope Measurements. Experiments were performed in a microfluidic channel depicted in Figure 2 and constructed using the toner transfer method as described previously.[13] Microfluidic channel construction is described further in the Supporting Information.

Fiber bundles were placed on the polydimethylsiloxane (PDMS) substrate positioned channel side up. The channel width and depth were selected to provide optimal access to solution and minimal compression to hold the activated fiber isometric. The PDMS substrate with a mounted fiber was inverted channel side down and placed on a clean glass coverslip. The PDMS made a spontaneous watertight seal, and the relaxing solution was immediately passed through the channel. The sample was then ready for microscope experiments.

Connective tissue present in the bundle adhered to the large surface area presented by the microscopically rough PDMS surface, allowing a minimum of compression to immobilize the contracting fiber. Fiber length was observed before and after single-molecule TIRF measurements to check for length change. Experiments were terminated when the fiber was shortened by more than ∼5% from the starting resting length.
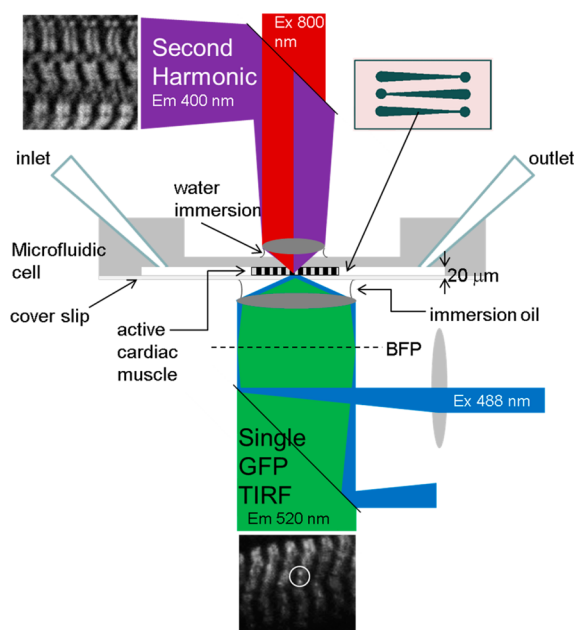
Figure 2. TIRF observation characterizes single myosin lever arms in the muscle fiber using exchanged HCRLC-PAGFP. TIRF excitation uses 488 nm laser light focused on the back focal plane (BFP) to excite photoactivated PAGFP that emits with a peak intensity at 520 nm. Infrared (800 nm) light focused on the fiber causes myosin SHG to image the periodic myosin structure and monitor sarcomere length. The microfluidic chamber was constructed from a brass master etched into the pattern shown in the inset. Three channels were constructed with depths of 20 (shown) to 40 μm to accommodate different fiber bundle sizes and to apply mild pressure on the contracting fiber to keep it stationary during observation. The channel is also the conduit to exchange solutions. TIRF and SHG experiments were performed sequentially.

Following single-molecule experiments using TIRF on the inverted wide field microscope, the chamber was immediately taken to the upright scanning 2 photon microscope for measurement of the SHG signal.

Microscopy. Figure 2 shows excitation and emission pathways for the TIRF widefield microscope (Olympus IX71) and the multiphoton excitation (MPE) scanning upright microscope (Olympus FV1000 and BX61) for SHG. Experiments were conducted sequentially, first the TIRF experiments using a 100×, 1.49 NA oil immersion objective and then the SHG experiments using a 25×, 1.05 NA water immersion objective. The water immersion objective has a 2 mm working distance to image the fiber through 1 mm of PDMS.

The single-molecule TIRF microscope setup using photoactivatable probes is identical to that described previously.[3,4] Experiments involve axial scanning by image space camera translation. A microscope stage with leadscrew drives and stepper motors (LEP, Hawthorne, NY) translate the EMCCD camera (C9100-13, Hamamatsu, Hamamatsu, Japan) with submicrometer resolution. The quantitatively analyzed axial-scanned imagery contained five frames in a scene covering 1 mm in image space or 100 nm in object space. The five frames take 5 s to collect with ~40 and 60% of the time interval used to reposition the camera and collect photons, respectively. Images span 4.6 s of real time because the final camera translation is irrelevant. The porcine left ventricle papillary cardiac muscle fibers used here contain predominantly the β-cardiac myosin heavy chain isoform. The β-cardiac myosin has

cycling kinetics 2−10-fold slower than that of the α-cardiac isoform.[14,15] Isometric α-cardiac cross-bridges in permeabilized transgenic mouse myofibrils cycle with a periodicity of ~3 s,[16] suggesting the cross-bridges observed here are approximately static during the 4.6 s data collection time interval. Two photoactivated single myosins are circled in the representative TIRF image of the active isometric permeabilized papillary fiber shown in Figure 2, where 488 nm illumination produces PAGFP emission at ~520 nm.

SHG from striated muscle originates from thick filament myosin rod domains but not S1.[17] SHG images were collected from the permeabilized papillary cardiac muscle fibers used in the single-molecule experiments to estimate and compare sarcomere length from relaxed and isometric active fibers. SHG images were Fourier transformed and the spatial frequencies compared as described in the Supporting Information. A representative SHG image of a relaxed permeabilized papillary fiber is shown in Figure 2, where 800 nm illumination produces the ~400 nm back-scattered SHG image. After SHG imaging, fibers were removed from the microfluidic chamber and placed in the activating solution to qualitatively test contractility. Fibers were normally shortened to approximately half the starting length.

Photoselection by Photoactivation. Total probe molecules N convert from unphotoactivated (N_B) to photoactivated (N_A) species by irreversible isomerization, $N_B \leftrightarrow N_A$, as described previously.[4] Experiments utilized sparse photoactivation to obtain the highest possible directional ordering in photoactivated probes. Measuring the emission dipole orientation of the photoactivated species is the goal accomplished with emission spatial pattern analysis.

Interpretation of Single-Molecule Emission Patterns. Light collected by the objective forms a real image of the emitter dipole on the CCD detector. The image is a three-dimensional pattern that devolves into six basis patterns with coefficients that depend algebraically on the dipole orientation. Given the basis patterns, we invert an observed image to deduce the coefficients by using maximum likelihood fitting for Poisson-distributed uncertainties. The coefficients establish a 1:2 correspondence between pattern and dipole moment orientations because a particular dipole and its spatial inversion produce the same emission pattern.[3,4] Dipole moment orientation is represented by coordinates (β,α) for β, the spherical polar angle, and α, the azimuth in muscle fiber coordinates where the z-axis is parallel to the fiber symmetry axis, the x-axis is in the plane of the coverslip where total internal reflection occurs (TIR interface), and the y-axis is normal to the coverslip plane pointing into the aqueous medium. Inversion symmetry implies (β,α) and ($\pi-\beta,\alpha+\pi$) are equivalent; hence, the entire solution set of dipole orientations can be shown on the domain defined by $0 \leq \beta \leq \pi$ and $0 \leq \alpha \leq \pi$. P-Polarization illumination, with the electric field predominantly oriented normal to the TIR interface and the fiber symmetry axis, is used for photoactivation and emission excitation.[18]

Single-molecule emission is documented by five images in a scene covering lateral and axial dimensions of the pattern. When analyzed, each five-image scene converts to the emission dipole moment orientation coordinates (β,α). We recorded scenes from fibers in rigor, relaxation, and isometric contraction at room temperature. Each physiological state was characterized by $\geq$48 dipole coordinates ($\geq$96 including those related by

inversion symmetry) for PAGFP-tagged WT, M20L, E134A, and G162R HCRLC exchanged cross-bridges.

Principal Angle. We investigate cross-bridge rotation for force production during contraction by assuming the HCRLC-PAGFP rotates as a rigid body and computing principal angle transitions between single lever arm fixed probe dipoles. Unit vector $\hat{v}$ represents a single dipole orientation computed from coordinates (β, α) using $\hat{v} = \{\sin[\beta]\cos[\alpha], \sin[\beta]\sin[\alpha], \cos[\beta]\}$. Let vectors $\hat{v}_i$ and $\hat{u}_j$ represent the ith and jth unit dipoles, respectively, for a set of molecules, and then the principal angle transition between them is given by

$$\Phi_{i,j}(\{\hat{v}\}, \{\hat{u}\}) = \arccos(\hat{v}_i \cdot \hat{u}_j) \tag{1}$$

Sets $\{\hat{v}\}$ and $\{\hat{u}\}$ are observed from the same fiber physiological state representing orientation dispersion or from different physiological states representing state transition.

Figure 3 shows a schematic cross-bridge cycle and the meaning of the principal angle-state transition, Φ, relating lever
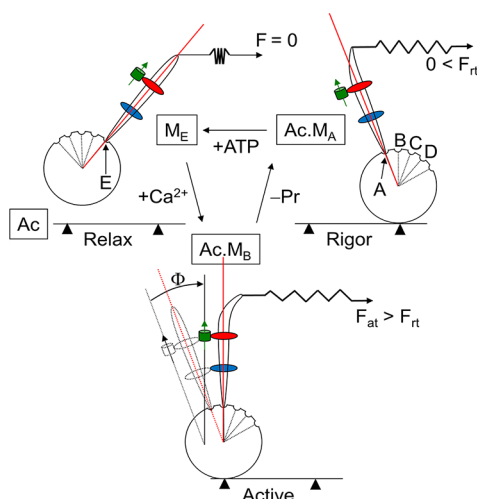
Figure 3. Simplified cross-bridge cycle in contraction detailing myosin's discrete substates (A−E) and their correspondence to lever arm orientation. The rigor cross-bridge binds actin (Ac) in the A-state (M_A), exerts force F_{rt}, and maintains the PAGFP (green cylinder with arrow)-tagged HCRLC (red) in the A-state orientation. ELC is colored blue. The addition of ATP relaxes the fiber via the ATP binding to myosin and detaching actin. The relaxed cross-bridge assumes the E-state (M_E) with the lever arm reprimed for a new power stroke. Ca^{2+} addition activates the fiber producing force F_{at}. In isometric contraction, single lever arms assume one of their intermediates (A−E) depicted here as M_B, which is a high-force producing intermediate having a characteristic orientation indicated by Φ.

arm positions. A myosin cross-bridge in rigor supports significant rigor tension, F_{rt}, with the lever arm strained and in the minimum free energy A-state. ATP binding releases the cross-bridge from actin and reprimes myosin forming the maximum free energy E-state in relaxation that is weakly actin bound and does not support tension. Addition of Ca^{2+} initiates contraction causing strong actin binding and lever arm rotation in the power stroke. The principal angle, Φ, describing the cross-bridge orientation transition between states is depicted in the figure. For the sake of simplicity, we represent the tension-generating lever arm swing movement in a plane also containing the PAGFP dipole moment, although this is unlikely to happen. The Φ amplitude is less than or equal to the real

lever arm principal swing angle amplitude, Ψ, because just a component of the PAGFP dipole moment lies in the lever arm swing plane. Thus, the Φ's correspond to a lower bound on Ψ. The free energy for the lever arm swing

$$\Delta G = \frac{1}{2}kh^2 \approx \frac{1}{2}kl^2 \tan^2 \Psi \tag{2}$$

as derived previously[4] and for spring constant $k \approx 2$ pN/nm in WT skeletal myosin,[19] step size $h \approx 5.2$ nm,[20] and lever arm length $l \approx 8.5$ nm.[21] Equation 2 implies that $\tan \Phi \leq h/l$ or that a Φ of $\leq 33°$ covers the power stroke. This is the Φ domain chosen for the Φ permutation and Φ density histograms defined and discussed subsequently.

Cross-Bridge Dispersion. Rigor cross-bridges are formed from a single turnover of ATP when they perform a final power stroke and then release product. Increasing tension in the fiber implies that cross-bridges releasing ATP hydrolysis products do not all reach their free energy minimum configuration contributing to rigor cross-bridge orientation dispersion (only the free energy minimum configuration is indicated in Figure 3). Increasing tension in the active isometric fiber implies that unsynchronized cross-bridges reach their stall force at various orientation states in the free energy pathway leading to active cross-bridge orientation dispersion.

The transitions from disperse active cross-bridges to the minimum free energy rigor cross-bridge are what we wish to identify and characterize. Hence, while active dispersion is an interesting part of the active-rigor principal angle transition, rigor dispersion is not. We identify the minimum free energy rigor orientation to minimize rigor dispersion in the active-rigor principal angle. The same concept applies to the relax-rigor principal angle. We introduce a selection rule to identify the minimum free energy rigor cross-bridge dipole orientation and a symmetry rule to sort dipoles into their half-sarcomere subsets. The rules promote the correct assignment of active dipole intermediates to their minimum free energy end point.

Dipole Orientation Selection and Symmetry Rules. Photoactivation photoselection selects a similarly oriented dipole set from all dipoles in the muscle fiber. Within the photoactivated set, dipole dispersion due to rigor tension produces a set of dipoles related to a unique minimum free energy conformation. If Φ describes the angular dispersion among single-lever arm fixed probe dipoles in rigor, we specify the set of all ordered pairs of single molecules in rigor $\{(\hat{v}_i, \hat{u}_j)\}$, with Φ falling into substates A−E with increasing Φ values (Figure 3). From the ordered pairs of single molecules, we identified each $\hat{u}_j$ in $\{(\hat{v}_i, \hat{u}_j)\}$ that has a transition to each of the B−E substates. This set of dipoles, always denoted $\hat{u}_j$, is the minimum free energy rigor A-state representing the power stroke end point. This is the selection rule.

Each $\hat{u}_j$ has an associated projection scalar

$$s_{i,j}(v, u) = (c_1\hat{x} + c_3\hat{z}) \cdot (\hat{v}_i \times \hat{u}_j) \tag{3}$$

for $\hat{v}_i$ dipoles qualifying $\hat{u}_j$ in the selection rule, and arbitrary constants c_1 and c_2 selected to avoid instances when $s_{i,j}(v,u) = 0$. Pseudovector $(\hat{v}_i \times \hat{u}_j)$ combines vectors related by a principal angle that falls within the A−E substates. Its projection onto the x- or z-axis will reverse sign in a y-axis rotation of the fiber through $180°$ that exchanges the half-sarcomeres. Requiring the sign of $s_{i,j}(v,u)$ to be conserved for every $\hat{v}_i$ qualifying $\hat{u}_j$ places $\hat{u}_j$ in a unique half-sarcomere. We find that for $c_1 = c_3 = 1/\sqrt{2}$, $s_j(v,u)$ is never zero and where we have dropped the first index because $s_j(v,u)$ specifies the half-sarcomere for $\hat{u}_j$ for all $\hat{v}_i$. We

also require active or relaxed isometric dipoles, $\hat{\mathbf{a}}_i$ or $\hat{\mathbf{r}}_i$, respectively, participating in the A–E configurations transitioning to $\hat{\mathbf{u}}_j$ to have a scalar $s_{i,j}(a,u)$ or $s_{i,j}(r,u)$, respectively, with a sign equal to the sign of $s_j(v,u)$. This is the symmetry rule requiring active-rigor or relax-rigor transitioning between dipoles in the same half-sarcomere.

The "Φ permutations" for active-rigor or relax-rigor transitions collect all instances of allowed transitions between dipoles. Active-rigor or relax-rigor allowed transitions are identified by ordered pairs $(\hat{\mathbf{a}}_i,\hat{\mathbf{u}}_j)$ or $(\hat{\mathbf{r}}_i,\hat{\mathbf{u}}_j)$, respectively. They amplify common relationships between dipoles in the two physiological states. The "Φ density" for active-rigor or relax-rigor transitions is a probability density. It sorts instances of the allowed transition between dipoles. The allowed $\hat{\mathbf{a}}_i$ or $\hat{\mathbf{r}}_i$ dipoles falling in the active or relaxed A-state are removed from the active or relaxed list such that they participate just once. The remaining active or relaxed $\hat{\mathbf{a}}_i$ or $\hat{\mathbf{r}}_i$ dipoles falling in the B-state are identified next and then also removed from the list. This process continues in sequence to the E-state.

Repetitive relationships in $(\hat{\mathbf{a}}_i,\hat{\mathbf{u}}_j)$ or $(\hat{\mathbf{r}}_i,\hat{\mathbf{u}}_j)$ will appear in either the Φ permutation or the Φ density. The Φ permutation has better statistics because the total number of instances is larger due to resampling because $\hat{\mathbf{a}}_i$'s or $\hat{\mathbf{r}}_i$'s occasionally qualify as allowed with more than one $\hat{\mathbf{u}}_j$. The Φ density $\hat{\mathbf{a}}_i$ or $\hat{\mathbf{r}}_i$ dipoles occur just once in their lowest-free energy allowed instance. If $\hat{\mathbf{a}}_i$ or $\hat{\mathbf{r}}_i$ aligns by coincidence with two or more $\hat{\mathbf{u}}_j$'s, it could be incorrectly assigned in the Φ density. We cannot rule out this possibility without direct knowledge of the $\hat{\mathbf{a}}_i$ or $\hat{\mathbf{r}}_i - \hat{\mathbf{u}}_j$ correspondence by tracking a single molecule through each physiological state, but this circumstance is impractical and undesirable for reasons already mentioned. However, incorrect assignment is unlikely given the high selectivity of probe photoactivation, the selection rule as applied to $\hat{\mathbf{u}}_j$, and the symmetry rule agreement between $\hat{\mathbf{a}}_i$ or $\hat{\mathbf{r}}_i$ and $\hat{\mathbf{u}}_j$.

■ RESULTS

Fiber Tension Measurements. Isometric tension follows linearly light chain extraction and reconstitution of untagged and PAGFP-tagged WT HCRLC in permeabilized porcine papillary muscle fibers.[4,11] We showed that peak tension declines with endogenous RLC removal and recovers with its replacement. We also showed that extracting conditions (with magnesium chelator CDTA) efficiently remove endogenous light chain while inducing a small fraction of irreversibly actin-bound myosin (dead heads). We measured an ∼20% decline in the peak isometric tension by treatment with extracting conditions without CDTA when there is no endogenous RLC removal. Hence, peak isometric tension recovery of ≥80% indicates a full recovery of tension following light chain extraction and reconstitution. Table 1 summarizes isometric tension measurements for reconstituted fibers where $1 - T_{ex}/T_0$ measures the endogenous RLC extracted fraction for T_{ex}, the tension after extraction, and T_0, the tension before extraction. The endogenous RLC extraction efficiency averages to ∼50%. The normalized reconstituted tension T_{rc}/T_0 represents the exchange efficiency provided the exchanged HCRLC supports full isometric tension. Mutants considered here fully recover tension when exchanged except for E134A and E134A-PAGFP that lose ∼10 and ∼15% of peak tension, respectively.

Figure 4 shows the SDS–PAGE gel for native RLC extraction and reconstitution with (human MYL2 mutant) E134A-PAGFP, where lanes 1 and 2 contained control and reconstituted fibers, respectively, and lane 3 contained reference

Table 1. Papillary Muscle Fiber Isometric Tension[a]

| HCRLC variant	extracted fraction $(1 - T_{ex}/T_0)$	tension recovery (T_{rc}/T_0)	n
WT	0.53 ± 0.09	0.85 ± 0.03	5, 4[b]
M20L	0.51 ± 0.1	0.86 ± 0.05	3
E134A	0.54 ± 0.04	0.75 ± 0.01	4
G162R	0.53 ± 0.02	0.91 ± 0.03	4
WT-PAGFP	0.48 ± 0.04	0.84 ± 0.03	10
M20L-PAGFP	0.50 ± 0.04	0.88 ± 0.03	6
E134A-PAGFP	0.52 ± 0.04	0.71 ± 0.03	8
G162R-PAGFP	0.48 ± 0.02	0.84 ± 0.02	11

[a]T_0 is the initial tension, T_{ex} the tension after extraction, and T_{rc} the tension measured after extraction and reconstitution of the HCRLC variants. The average T_0 is 155 ± 20 kN/m^2 for the fibers tested. A tension recovery of ≥80% indicates full recovery (see Fiber Tension Measurements). Errors are standard errors of the mean for n experiments. [b]One fiber broke during reconstitution.
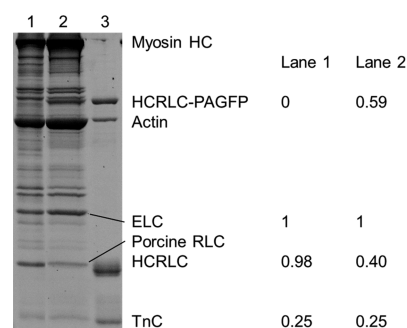
Figure 4. SDS–PAGE of the fiber protein extract and purified proteins. Lane 1 contained the untreated fiber control, lane 2 the E134A-PAGFP exchanged fiber, and lane 3 purified proteins identified on the right of the gel except for ELC and porcine RLC. Quantitative evaluation of the untreated and exchanged fibers was conducted with ImageJ and using the ELC content as the standard. The error is ∼10%. Stoichiometric replacement of the porcine RLC is indicated by the sum of lane 2 bands at HCRLC-PAGFP and porcine RLC equaling 1 within error. HC is heavy chain, and TnC is troponin C.

purified proteins. Protein molar concentrations listed to the right are normalized relative to essential light chain (ELC). The ELC is not affected by the extraction−reconstitution treatment. Extraction removes 58% of the endogenous RLC, and the level of reconstitution is 100% with the tagged human mutant. The fiber tension data for E134A and E134A-PAGFP taken together with the SDS−PAGE data from extracted proteins indicated E134A inhibits peak isometric tension. The other mutants do not affect peak isometric tension. SDS−PAGE of WT and other mutants confirms exchange efficiencies of ∼50% and our ability to fully replace extracted endogenous RLC with the recombinant HCRLC or HCRLC-PAGFP.

Single-Molecule Measurements. We measure single lever arm orientation as described in Methods. Figure 5 shows scatter plots for single dipole coordinates, (β,α), in WT and M20L species measured from fibers in rigor (filled blue square), isometric contraction (filled red square), and relaxation (empty blue square). Scatter plots for all species (WT, M20L, E134A, and G162R) are compared in Figure S3 of the Supporting Information. Extremes in the (β,α) domain, and in the central region where $(\beta,\alpha) \approx (90,90)$, are unpopulated by cross-bridges in all states. The extremes are excluded by photoselection from p-polarization photoactivation light that favors $\langle \beta \rangle \approx \langle \alpha \rangle \approx 90°$. The central depletion zone is from
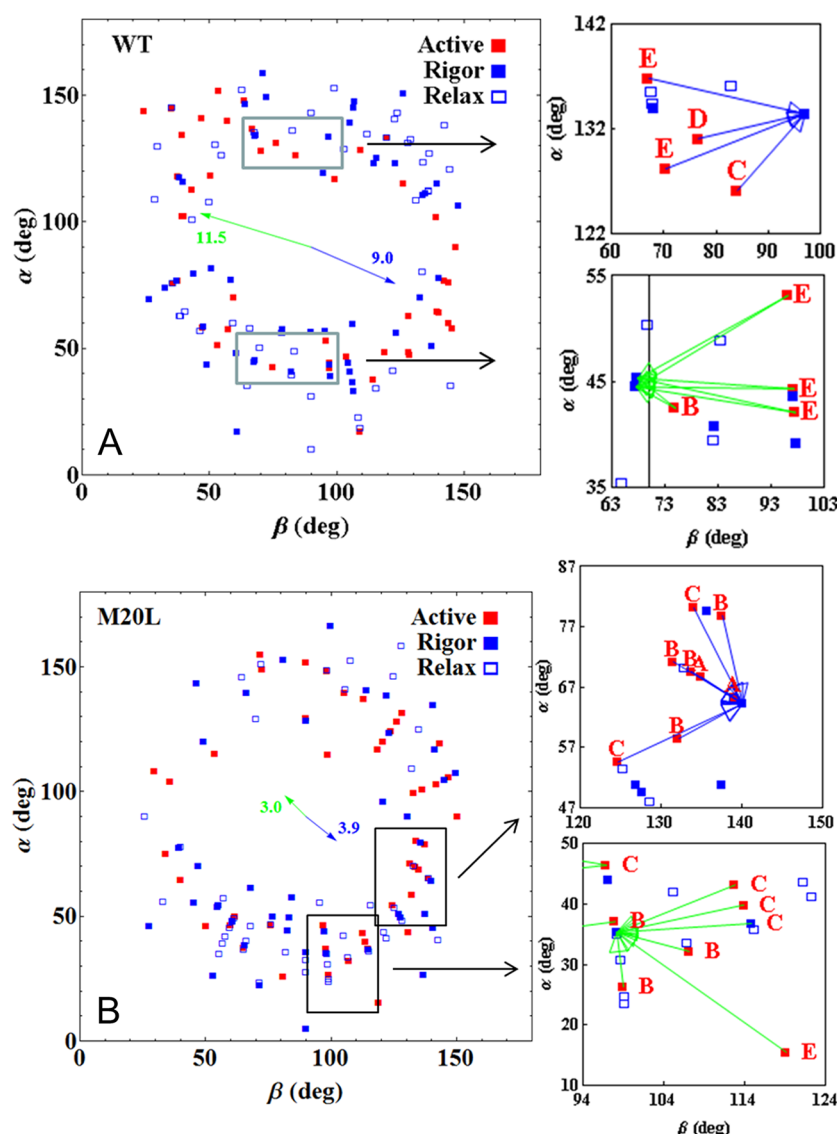
Figure 5. Dipole moment spherical polar coordinate (β,α) scatter plot for fibers in rigor (filled blue square), isometric contraction (filled red square), and relaxation (empty blue square) and for the WT and M20L species. Coordinates are defined relative to a lab frame z-axis parallel to the fiber symmetry axis, the x-axis in the plane of the coverslip, and the y-axis normal to the coverslip plane pointing into the aqueous medium. Right panels show enlargements of the rectangular regions in the scatter plots. They depict the arrow clusters associating various high-free energy active isometric coordinates in substates A−E (Figure 3) at the base of the arrow with their unique minimum free energy rigor A-state at the pointy ends. Blue or green arrows designate a positive or negative projection scalar, respectively (eq 3). Arrow clusters like those in the enlargements populate the entire scatter plot but were left out here for the sake of clarity. The full set of clustered arrows for WT and all mutant species is shown in Figure S3 of the Supporting Information. Blue and green arrows arranged like the hands of a clock are the average orientations of all the same colored clustered arrows (including those not shown here outside of the rectangles). They are in the text termed $\overrightarrow{\Delta g}(\pm)$ and have amplitudes proportional to the average free energy separating the isometric active cross-bridge from the minimum free energy rigor A-state cross-bridge computed using eq 2.

steric/molecular-crowding constraints that depopulate the central zone in favor of orientations that allow strong interaction with actin because favorable regions are roughly equivalent in rigor, active, and relaxation. The steric/molecular-crowding constraints originate from the thick filament.[4] The average dipole orientation in each physiological state (active isometric, rigor, or relax) includes contributions from both half-sarcomeres and does not vary for WT and mutant species beyond a standard deviation. The standard deviations (σ) themselves are similar for all cases but differ with respect to the degree of freedom such that $\sigma_\beta \sim 36°$ and $\sigma_\alpha \sim 43°$, so that all the scatter plots are ellipsoidal with a slightly longer dimension on the α-axis.

Selected portions of the scatter plots in Figure 5 are enlarged to show the principal rotation relationship between active and minimum free energy rigor A-state coordinates identified as described in Methods. Enlarged portions contain arrow clusters associating several high-free energy active isometric coordinates in substates A−E (Figure 3) with a unique minimum free energy rigor A-state. Blue and green arrows designate the $\pm$ symmetry (eq 3), indicating the half-sarcomere dipole location. WT active-rigor transition clusters rotate from higher-free energy substates using mostly the β degree of freedom, while M20L active-rigor transition clusters rotate from lower-free energy substates using more the α degree of freedom. This observation is quantified by the diverging blue and green arrows

arranged like the hands of a clock in the middle of the scatter plots in Figure 5 and denoted here as $\overrightarrow{\Delta g}(\pm)$. They are the average orientations of all the same colored clustered arrows (including those not shown here outside of the rectangles) and have amplitudes proportional to the average free energy separating the isometric active coordinate from the minimum free energy rigor A-state coordinate computed using eq 2 in units of piconewtons per nanometer with a standard error of the mean of <25%. Because $\Psi \geq \Phi$, eq 2 estimates a lower bound on the free energies; however, the relative amplitudes of $\overrightarrow{\Delta g}(\pm)$'s from WT and M20L species are estimated without ambiguity assuming the relationship between Ψ and Φ does not change among WT and mutant species (discussed below). The free energy depicted by the $\overrightarrow{\Delta g}(\pm)$ amplitude for the mutant species shown in Figure 5 anticipates their altered relative stiffness (affecting k in eq 2) as estimated below. The $\overrightarrow{\Delta g}(\pm)$ orientation is qualitative because of the outliers; however, the trend between WT and all mutants is consistent. All arrow clusters and $\overrightarrow{\Delta g}(\pm)$'s for the fiber species are shown in Figure S3 of the Supporting Information.

The $\overrightarrow{\Delta g}(\pm)$'s are shorter and rotate clockwise in the mutant compared to those in WT species. The $\overrightarrow{\Delta g}(\pm)$ length change indicates the mutant isometric active cross-bridge occupies lower-free energy substates compared to WT. $\overrightarrow{\Delta g}(\pm)$ rotation indicates the mutant isometric active cross-bridge undergoes a smaller polar but larger azimuthal angular change as active substates undergo the transition to the minimum free energy rigor A-state configuration. If this is placed in the context of a cross-bridge cycle, force without work production happens quickly as relaxed cross-bridges are activateed and stretch their elastic element against resisting force. Work production follows as resisting force yields, allowing filament sliding and the completion of the cross-bridge cycle. Figure 5 and Figure S3 of the Supporting Information characterize the work production phase. Mutants have diminished work production $[\overrightarrow{\Delta g}(\pm)$ amplitude)] accompanying the cross-bridge active-rigor transition. The reduced work production correlates with a reduced polar and increased azimuthal angular change $[\overrightarrow{\Delta g}(\pm)$ orientation], suggesting the free energy liberated by motor domain ATPase is partially dissipated in the mutant by unproductive or counterproductive azimuthal rotation.

Figure 6 shows the Φ permutation for active-rigor transitioning. We chose states A–E corresponding to the following ranges: $0 \leq \Phi < 7$, $7 \leq \Phi < 12$, $12 \leq \Phi < 20$, $20 \leq \Phi < 27$, and $27 \leq \Phi < 33$, respectively. These choices are somewhat arbitrary, but they provide the framework for the discussion. Discretized Φ permutations are apparent in each species except E134A. The latter has a relatively featureless Φ permutation, while the other mutants lose their discreteness after the C-state. Figure 7 contrasts Φ permutations for active-rigor and relax-rigor transitions from WT HCRLC-PAGFP. Φ permutations are relatively featureless in relax-rigor compared to active-rigor transitioning, implying angular discreteness is introduced by actin binding. The lack of discreteness in E134A active-rigor transitioning (Figure 6), its similarity to WT relax-rigor transitioning (Figure 7), and the unique loss of peak isometric tension in E134A (Table 1) together suggest E134A
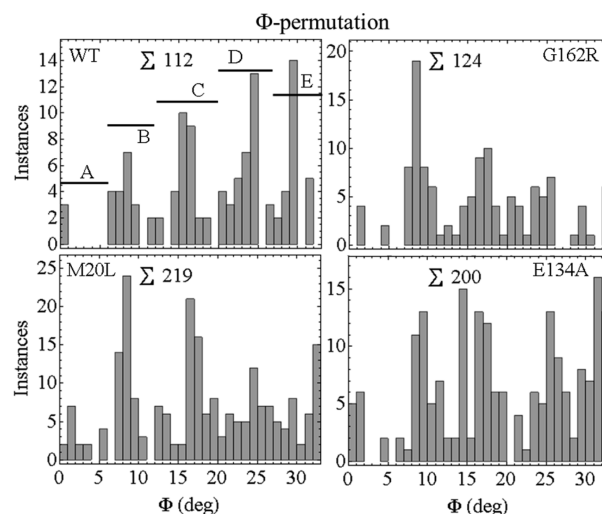
Figure 6. Φ permutations for the active-rigor transitions in WT and mutant HCRLC-PAGFP exchanged permeabilized papillary muscle fibers. The histogram is discretized corresponding to A- to E-state intermediates. $\sum$ indicates total instances.
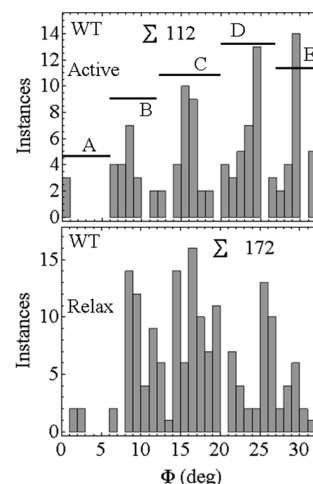

Figure 7. Φ permutations for the active-rigor (Active) and relax-rigor (Relax) transitions in WT HCRLC-PAGFP exchanged permeabilized papillary muscle fibers. $\sum$ indicates total instances.

affects actin binding in contraction. Dipole orientation within the discretized packets of the Φ permutations is constant among WT and mutant species (excluding E134A), implying the relationship between Φ and Ψ does not change among species.

The Φ density in an active isometric fiber is a subset of the Φ permutation computed as described in Methods. The Φ densities for the WT, G162R, M20L, and E134A HCRLC-PAGFP exchanged fibers are indicated in Figure 8. The occupation probabilities for substates A–E are derived from the Φ densities by summing instances over the angular substate domains and then dividing by the total instances to give probability. Occupation probabilities listed in Table 2 show the distinctiveness of the WT and mutant isoforms. They quantitate the trend evident in Figure 8 that Φ density shifts toward the lower free energy end of the power stroke upon introduction of mutant HCRLC-PAGFP. Φ density loss at the high-free energy end explains the concomitant loss of the discretized orientation feature at the high-free energy end for
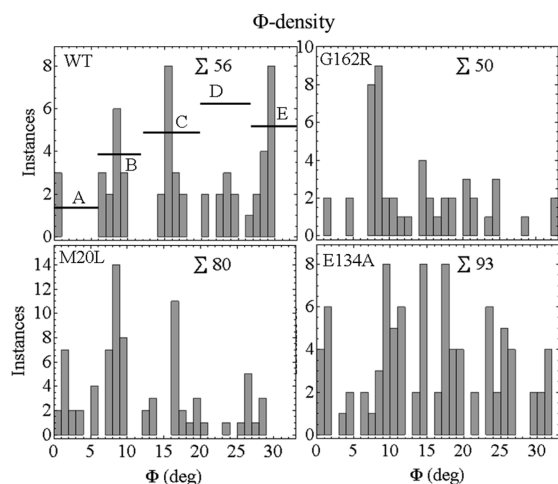
Figure 8. Φ densities for single myosins in an isometric active fiber. The WT and mutant species maintain different Φ densities in isometric contraction. The altered intermediate densities reflect reduced lever arm stiffness caused by mutation in HCRLC. The E134A mutant also has smaller isometric tension (Table 1). $\sum$ indicates total instances.

the mutants other than E134A seen in the Φ permutations in Figure 6.

Lever arm displacement generating tension is measured at the distal end and is proportional to $\Phi_E - \Phi_i$, where Φ_E is for the E-state configuration where the lever arm exerts no force and subscript i is the ordinate in Figure 8. Isometric force F

$$F = \frac{kl \sum_i \rho_i (\Phi_E - \Phi_i)}{\sum_i \rho_i} \tag{4}$$

for k the lever arm spring constant or stiffness already mentioned in eq 2 and ρ_i the Φ density from Figure 8. We normalize F/l to the WT level and then use eq 4 to estimate relative stiffness k. Stiffness is significantly lower in the mutant isoforms than in WT. The order of stiffness is as follows: WT > G162R > E134A ≈ M20L. G162R stiffness is intermediate and unlike either WT or the lower-stiffness mutants. E134A also has a lowered isometric tension that affects stiffness separately from occupation probability.

SHG Measurements. In a few cases, and following single-molecule experiments using TIRF, the microfluidic chamber containing the fiber was immediately taken to the two-photon upright scanning microscope for SHG measurements. Repre-

sentative data are shown in Figure 2 and Figure S2 of the Supporting Information. SHG images imply relaxed and active fibers have a similar average sarcomere spacing of 2.33 μm. Otherwise, sarcomere spacing was estimated from TIRF images giving equivalent results. SHG imaging has deep penetration and a long depth of focus in contrast to TIRF, providing contrasting information from deep versus surface sarcomeres about fiber integrity following contraction−relaxation cycles.

■ DISCUSSION

Single-myosin detection in the muscle fiber lattice involves its isolation in a condensed phase where each myosin occupies a volume of <10 zL (10^{-21} L). Sparse labeling techniques are undesirable in this application because how the probe affects fiber function, in this case, isometric contraction, cannot be assessed when significantly less than 50% of the myosin is modified. HCRLC-PAGFP permits single-molecule detection using sparse photoactivation of PAGFP, while the level of our exchange with the endogenous RLC is >50% (Table 1). We developed the analytical tools to uniquely and precisely deduce PAGFP orientation by exploiting the full information content in the three-spatial dimension fluorescence emission pattern.[3] These tools provided the single dipole coordinates shown in Figure 5 and Figure S3 of the Supporting Information. We found previously that in this system molecular-crowding and lattice constraints dominate the energy landscape, limiting myosin rotational movement to a domain favoring actin interaction.[4]

Disease-implicated mutation suggests a genetic origin for illness, although the pathway linking the diminished mutant protein function and the illness phenotype has proven to be neither simple nor direct. Nonetheless, a genetic origin to clinically diagnosed HCM appears to select the most severely ill, indicating a practical reason to identify the protein function affected by the mutant.[6] Furthermore, characterizing myosin functionality and its alteration by disease-implicated mutation is the only rational means of elucidating the molecular basis for disease and identifying the targets for smarter therapy. Heart disease is linked genetically to several cardiac sarcomere proteins, including HCRLC. HCRLC binds and stabilizes the heavy chain for folding and function.[22] Disease-linked RLC mutations R58Q and N47K were shown to perturb the strain sensitivity of ADP affinity.[2] The A13T mutant triggered a hypertrophic remodeling of the heart in transgenic mice despite a low level of incorporation into the cardiac tissue, suggesting its effect is nonlinear.[23]

Table 2. Substate Occupation Probabilities, Maximum Isometric Tensions, and Cross-Bridge Stiffnesses for HCRLC-PAGFP Exchanged Permeabilized Papillary Muscle Fibers[a]

state	WT	M20L	E134A	G162R
A	0.054 ± 0.003	0.22 ± 0.04	0.128 ± 0.002	0.08 ± 0.03
B	0.25 ± 0.07	0.35 ± 0.10	0.28 ± 0.01	0.44 ± 0.07
C	0.26 ± 0.05	0.28 ± 0.02	0.31 ± 0.02	0.24 ± 0.02
D	0.18 ± 0.02	0.11 ± 0.06	0.20 ± 0.04	0.18 ± 0.06
E	0.25 ± 0.01	0.05 ± 0.02	0.08 ± 0.04	0.06 ± 0.01
F_{at}	1	1.05 ± 0.07	0.85 ± 0.07	1.00 ± 0.06
relative stiffness	0.44 ± 0.02	0.32 ± 0.02	0.33 ± 0.01	0.35 ± 0.01

[a]Errors represent the standard error of the mean for three or four measurements. The full data set for single-molecule dipole orientations was partitioned into three or four parts, and then occupation probabilities were computed for each part. The n results were averaged, and the standard error of the mean was computed. F_{at} is the peak isometric tension normalized to the WT fiber value. Relative stiffness is computed using eq 4 and F_{at}.

We investigated three HCM-linked mutants of HCRLC. Figure 1 shows their locations in the β-cardiac myosin homology-modeled structure, and Figure 3 outlines the role of HCRLC in contraction. In isometric active fibers, the mutants cause a cross-bridge population inversion to higher-force-generating substates (Figure 8 and Table 2), while macroscopic isometric force is unchanged (M20L and G162R) or diminished (E134A). It implies the lever arms with bound mutant HCRLC strain more under shear force, requiring a larger lever arm rotation to achieve comparable isometric tension. We quantitated larger lever arm shear strain as diminished lever arm stiffness in Table 2. In free energy terms, the power stroke modification from WT caused by the mutants is indicated in Figure 5 and Figure S3 of the Supporting Information with the $\overrightarrow{\Delta g}(\pm)$ change in direction and amplitude. This alteration has the mutant lever arm dissipating the free energy liberated by ATP hydrolysis in the motor domain with azimuthal rotation that does not produce work, at the expense of polar rotation, which does. How these modifications affect cardiac muscle performance is unknown but can be framed in two testable hypotheses. The mutant lever arm preferentially populates lower-free energy substates in isometric contraction. Hypothesis 1 presumes these substates are stronger actin binders than the higher-free energy substates occupied by the WT lever arm. The former create internal drag on filament sliding by prolonging actin attachment in a normally low duty ratio motor inhibiting sliding and decreasing the myosin cycling rate. In the in vitro motility assay, a higher duty ratio enhances myosin's ability to move actin at a low surface density and a decreased myosin cycling rate lowers motility velocity. Alternatively, hypothesis 2 presumes the mutant power stroke cycle is nearly completed at peak force; hence, as the filament slides slightly under load, mutant lever arm myosin rapidly detaches from actin. The limited actin attachment time lowers the duty ratio and increases the myosin cycling rate. In the in vitro motility assay, the lower duty ratio weakens myosin's ability to move actin at a low surface density without altering the motility velocity because strong binding is normally just 5% of the unloaded cycle time so lowering it more has little impact.[24] In either hypothesis, mutant HCRLC alteration of myosin cycling, not related to the time myosin spends tightly bound to actin, will affect both the duty cycle and the motility velocity in the in vitro motility assay. Faster cycling will increase the duty cycle and motility velocity, while slower cycling will lower the duty ratio and motility velocity. Each case has a motility assay fingerprint.

The enlarged heart muscle HCM phenotype is consistent with the mutant HCRLC lever arm modification that downmodulates the energy conversion efficiency such that mutant myosin converts more ATP for the same work done compared to WT. In this case, heart muscle mass compensation would alleviate the immediate problem that appears to be the course taken in humans. We note also that the effect of myosin inefficiency on fiber contractility is difficult to predict; hence, two divergent hypotheses are feasible. A lowered energy conversion efficiency up- or downregulates fiber contractility depending on ATPase and actin binding kinetics, explaining why there is uncertainty surrounding how HCM mutants affect myosin function. If fiber contractility is the readout, then up- and downregulation could be consistent with the same underlying malady of inefficient energy conversion. It is not surprising then that linking the diminished mutant protein function and the illness phenotype has proven to be difficult.

Animal (mouse) and computational modeling indicated a role for HCRLC phosphorylation in cardiac contraction regulation.[25] The proposed mechanisms involve facilitating the actomyosin interaction by repositioning the myosin head in thick filaments[26] and the inhibition of myosin cycling kinetics due to increased lever arm stiffness.[27] The latter was associated with a larger duty ratio increasing the time myosin spends strongly actin bound, thereby slowing the ATPase cycle in studies conducted in vitro. Lower lever arm stiffness in the M20L, E134A, and G162R mutants can then be reasonably associated with a more rapid myosin cycling kinetics consistent with results of the in vitro motility of different HCM-implicated mutants of HCRLC.[28] This is tested for our mutants by the in vitro motility assay mentioned in hypotheses 1 and 2. Fortunately, the lever arm stiffness changes caused by our mutations and phosphorylation[25] are reciprocal, indicating a therapy for mitigating the effect of M20L, E134A, or G162R is HCRLC phosphorylation.

M20L and E134A contrast with G162R, suggesting that the position of the mutation in the HCRLC matters. In the latter, tension-generating substate populations more modestly reconfigure with the A-state minimally and approximately equally populated in both WT and G162R. It appears that M20L or G162R myosin compensates for the effect of mutation and produces maximum isometric force with below normal lever arm stiffness by radically or modestly reconfiguring substate populations. Radical reconfiguration in M20L reinforces the suggestion that light chain modification in the N-terminus near Ser15 affects function. E134A is not able to maintain normal isometric force or normal stiffness. On the basis of data reported here, actin binding in contraction is compromised by the E134A mutation.

Single-molecule studies in tissues present unique technical challenges that we have addressed with innovative device design. Evanescent illumination using TIRF selectively excites chromophores within ~100 nm of the glass coverslip−aqueous interface, enhancing the signal-to-noise ratio by minimizing background light.[29] However, coercing the dissected sample into the evanescent field is challenging because the dissected cardiac muscle fibers also contain significant connective tissue that frequently replaces muscle within the evanescent illumination. In addition, activated fibers often lift off the coverslip as they move slightly before reaching maximum tension. The microfluidic chamber provides an external and controllable constraint for confining part of the fiber to the illuminated volume, for keeping it immobilized during contraction, and as the means to exchange bathing solution with pressurized flow through the chamber. Our device was designed to allow access by an upright microscope where we can observe SHG from the muscle thick filaments to assess sarcomere length and evaluate fiber integrity before and after the rigor−relaxation−contraction cycles in the single-molecule experiments.

Single-molecule studies of the intact contractile system offer the uniqueness of single-molecule measurement in the apposite context of the intact muscle fiber. Proper context may be critical for deciphering an elusive molecular mechanism for HCM providing the best means available to identify the targets for a smarter therapy.

■ ASSOCIATED CONTENT

ⓢ Supporting Information

Detailed descriptions for construction of the microfluidic device appearing in Figure 2 and for the Fourier analysis of SHG images to measure sarcomere length in fibers and additional data in the form of dipole moment spherical polar coordinates for the mutant and WT species. This material is available free of charge via the Internet at http://pubs.acs.org.

■ AUTHOR INFORMATION

Corresponding Author

*Department of Biochemistry and Molecular Biology and Department of Physiology and Biomedical Engineering, Mayo Clinic Rochester, Rochester, MN 55905. Telephone: (507) 284-8120. Fax: (507) 284-9349. E-mail: burghardt@mayo.edu.

Notes

The authors declare no competing financial interest.

■ ACKNOWLEDGMENTS

■ REFERENCES

(1) Pant, K., Watt, J., Greenberg, M., Jones, M., Szczesna-Cordary, D., and Moore, J. R. (2009) Removal of the cardiac myosin regulatory light chain increases isometric force production. *FASEB J. 23*, 3571−3580.

(2) Greenberg, M. J., Kazimierczak, K., Szczesna-Cordary, D., and Moore, J. R. (2010) Cardiomyopathy-linked myosin regulatory light chain mutations disrupt myosin strain-dependent biochemistry. *Proc. Natl. Acad. Sci. U.S.A. 107*, 17403−17408.

(3) Burghardt, T. P. (2011) Single Molecule Fluorescence Image Patterns Linked to Dipole Orientation and Axial Position: Application to Myosin Cross-Bridges in Muscle Fibers. *PLoS One 6*, e16772.

(4) Burghardt, T. P., Josephson, M. P., and Ajtai, K. (2011) Single myosin cross-bridge orientation in cardiac papillary muscle detects lever-arm shear strain in transduction. *Biochemistry 50*, 7809−7821.

(5) Burghardt, T. P., and Ajtai, K. (2010) Single-molecule fluorescence characterization in native environment. *Biophys. Rev. 2*, 159−167.

(6) Olivotto, I., Girolami, F., Ackerman, M., Nistri, S., Bos, J. M., Zachara, E., Ommen, S. R., Theis, J. L., Vaubel, R. A., Re, F., Armentano, C., Poggesi, C., Torricelli, F., and Cecchi, F. (2008) Myofilament protein gene mutation screening and outcome of patients with hypertrophic cardiomyopathy. *Mayo Clin. Proc. 83*, 630−638.

(7) Josephson, M. P., Sikkink, L. A., Penheiter, A. R., Burghardt, T. P., and Ajtai, K. (2011) Smooth muscle myosin light chain kinase efficiently phosphorylates serine 15 of cardiac myosin regulatory light chain. *Biochem. Biophys. Res. Commun. 416*, 367−371.

(8) Ni, S., Hong, F., Haldeman, B. D., Baker, J. E., Facemyer, K. C., and Cremo, C. R. (2012) Modification of Interface between Regulatory and Essential Light Chains Hampers Phosphorylation-dependent Activation of Smooth Muscle Myosin. *J. Biol. Chem. 287*, 22068−22079.

(9) Burghardt, T. P., Ajtai, K., Chan, D. K., Halstead, M. F., Li, J., and Zheng, Y. (2007) GFP Tagged Regulatory Light Chain Monitors Single Myosin Lever-Arm Orientation in a Muscle Fiber. *Biophys. J. 93*, 2226−2239.

(10) Burghardt, T. P., Li, J., and Ajtai, K. (2009) Single Myosin Lever-Arm Orientation in a Muscle Fiber Detected with Photo-activatable GFP. *Biochemistry 48*, 754−765.

(11) Szczesna-Cordary, D., Guzman, G., Ng, S. S., and Zhao, J. (2004) Familial hypertrophic cardiomyopathy-linked alterations in Ca^{2+} binding of human cardiac myosin regulatory light chain affect cardiac muscle contraction. *J. Biol. Chem. 279*, 3535−3542.

(12) Dweck, D., Reyes-Alfonso, A., and Potter, J. D. (2005) Expanding the range of free calcium regulation in biological solutions. *Anal. Biochem. 347*, 303−315.

(13) Easley, C. J., Benninger, R. K., Shaver, J. H. H. W. S., and Piston, D. W. (2009) Rapid and inexpensive fabrication of polymeric microfluidic devices via toner transfer masking. *Lab Chip 9*, 1119−1127.

(14) Locher, M. R., Razumova, M. V., Stelzer, J. E., Norman, H. S., and Moss, R. L. (2011) Effects of low-level α-myosin heavy chain expression on contractile kinetics in porcine myocardium. *Am. J. Physiol. 300*, H869−H878.

(15) Rossmanith, G. H., Hoh, J. F. Y., and Kwan, L. J. (1986) Influence of V1 and V3 isomyosins on the mechanical behaviour of rat papillary muscle as studied by pseudo-random binary noise modulated length perturbations. *J. Muscle Res. Cell Motil. 7*, 307−319.

(16) Muthu, P., Mettikolla, P., Calander, N., Luchowski, R., Gryczynski, I., Gryczynski, Z., Szczesna-Cordary, D., and Borejdo, J. (2010) Single molecule kinetics in the familial hypertrophic cardiomyopathy D166V mutant mouse heart. *J. Mol. Cell. Cardiol. 48*, 989−998.

(17) Plotnikov, S. V., Millard, A. C., Campagnola, P. J., and Mohler, W. A. (2006) Characterization of the Myosin-Based Source for Second-Harmonic Generation from Muscle Sarcomeres. *Biophys. J. 90*, 693−703.

(18) Burghardt, T. P., and Thompson, N. L. (1984) Evanescent intensity of a focused gaussian light beam undergoing total internal reflection in a prism. *Opt. Eng. (Bellingham, WA, U.S.) 23*, 62−67.

(19) Uyeda, T. Q. P., Abramson, P. D., and Spudich, J. A. (1996) The neck region of the myosin motor domain acts as a lever arm to generate movement. *Proc. Natl. Acad. Sci. U.S.A. 93*, 4459−4464.

(20) Steffen, W., Smith, D., Simmons, R., and Sleep, J. (2001) Mapping the actin filament with myosin. *Proc. Natl. Acad. Sci. U.S.A. 98*, 14949−14954.

(21) Rayment, I., and Holden, H. M. (1993) Myosin subfragment-1: Structure and function of a molecular motor. *Curr. Opin. Struct. Biol. 1993*, 3944−3952.

(22) Lowey, S., Waller, G. S., and Trybus, K. M. (1993) Function of skeletal muscle myosin heavy and light chain isoforms by an in vitro motility assay. *J. Biol. Chem. 268*, 20414−20418.

(23) Kazmierczak, K., Muthu, P., Huang, W., Jones, M., Wang, Y., and Szczesna-Cordary, D. (2012) Myosin regulatory light chain mutation found in hypertrophic cardiomyopathy patients increases isometric force production in transgenic mice. *Biochem. J. 442*, 95−103.

(24) Uyeda, T. Q. P., Kron, S. J., and Spudich, J. A. (1990) Myosin step size: Estimation from slow sliding movement of actin over low densities of heavy meromyosin. *J. Mol. Biol. 214*, 699−710.

(25) Sheikh, F., Ouyang, K., Campbell, S. G., Lyon, R. C., Chuang, J., Fitzsimons, D., Tangney, J., Hidalgo, C. G., Chung, C. S., Cheng, H., Dalton, N. D., Gu, Y., Kasahara, H., Ghassemian, M., Omens, J. H., Peterson, K. L., Granzier, H. L., Moss, R. L., McCulloch, A. D., and Chen, J. (2012) Mouse and computational models link Mlc2v dephosphorylation to altered myosin kinetics in early cardiac disease. *J. Clin. Invest. 122*, 1209−1221.

(26) Levine, R. J., Chantler, P. D., Kensler, R. W., and Woodhead, J. L. (1991) Effects of phosphorylation by myosin light chain kinase on the structure of Limulus thick filaments. *J. Cell Biol. 113*, 563−572.

(27) Greenberg, M. J., Mealy, T. R., Watt, J. D., Jones, M., Szczesna-Cordary, D., and Moore, J. R. (2009) The molecular effects of skeletal muscle myosin regulatory light chain phosphorylation. *Am. J. Physiol. 297*, R265−R274.

(28) Greenberg, M. J., Watt, J. D., Jones, M., Kazmierczak, K., Szczesna-Cordary, D., and Moore, J. R. (2009) Regulatory light chain mutations associated with cardiomyopathy affect myosin mechanics and kinetics. *J. Mol. Cell. Cardiol. 46*, 108−115.

(29) Stout, A. L., and Axelrod, D. (1989) Evanescent field excitation of fluorescence by epi-illumination microscopy. *Appl. Opt. 28*, 5237−5242.